Local Yield and Compliance in Active Cell Monolayers

Austin Hopkins,[1,*] Michael Chiang,[2] Benjamin Loewe,[2] Davide Marenduzzo,[2] and M. Cristina Marchetti[1]
[1]Department of Physics, University of California Santa Barbara, Santa Barbara, California 93106, USA
[2]SUPA, School of Physics and Astronomy, University of Edinburgh, Peter Guthrie Tait Road, Edinburgh EH9 3FD, United Kingdom

(Received 8 March 2022; accepted 23 August 2022; published 27 September 2022)

The rheology of biological tissue plays an important role in many processes, from organ formation to cancer invasion. Here, we use a multiphase field model of motile cells to simulate active microrheology within a tissue monolayer. When unperturbed, the tissue exhibits a transition between a solidlike state and a fluidlike state tuned by cell motility and deformability—the ratio of the energetic costs of steric cell-cell repulsion and cell-edge tension. When perturbed, solid tissues exhibit local yield-stress behavior, with a threshold force for the onset of motion of a probe particle that vanishes upon approaching the solid-to-liquid transition. This onset of motion is qualitatively different in the low and high deformability regimes. At high deformability, the tissue is amorphous when solid, it responds compliantly to deformations, and the probe transition to motion is smooth. At low deformability, the monolayer is more ordered translationally and stiffer, and the onset of motion appears discontinuous. Our results suggest that cellular or nanoparticle transport in different types of tissues can be fundamentally different and point to ways in which it can be controlled.

DOI: 10.1103/PhysRevLett.129.148101

The dynamics of cells in dense tissues is important for understanding many biological processes, including embryonic development [1], cancer metastasis [2], and wound healing [3]. It underlies the epithelial-mesenchymal transition observed *in vivo* [4–6], in which stationary epithelial cells change to a more motile, mesenchymal phenotype. Experiments have also demonstrated a transition from glassy, or solidlike, to liquid dynamics in epithelial monolayers both *in vitro* [7–12] and *in vivo* [7,13]. Theoretical work on various models of dense tissues, including multiphase field [14], Voronoi [15,16], vertex [17–19], and cellular Potts models [20,21], has shown that this melting transition can be driven by the interplay of cell surface tension, cell motility, and active noise. An important question is whether the solid-to-liquid transition has an impact in tissue function in health and disease. Theory and experiments have begun to address this issue by exploring the rheological and mechanical properties of biological tissues, which have key consequences to their macroscopic biophysical behavior [13,22–31]. A mechanistic and quantitative understanding of the impact of cell surface tension and cell motility on the rheology and transport properties of biophysical tissues is, however, still lacking.

To shed light on this aspect, we study the local response of the tissue to the drag of an embedded colloidal probe. Constantly forced probes and oscillatory active microrheology [32] have been used to study the local material response in a wide variety of active and passive systems, including colloidal suspensions [33–37], biological tissues [23,38], and active disks [39–41]. While distinct from macrorheology that measures the material response on macroscopic scales, the two methods often yield qualitatively similar behavior when used to probe the rheology of complex fluids [42]. Active microrheology also provides a promising and nondestructive technique for understanding how cells in dense tissues generate spatially localized forces and transmit them to large scales.

Using a multiphase field model [14,43–50] of cells, we show that solidlike tissues exhibit a finite threshold for the onset of motion of an embedded probe pulled at a constant force. In passive systems of rigid particles, the existence of a finite threshold to probe motion correlates with a yield stress at the macroscopic scale [38]. Although no macrorheology data are available for our system, our finding suggests that our model tissue may behave as a yield stress material even in the presence of noisy cell motility [22,51]. A finite yield stress has indeed been reported in biological tissues [13] and in simulations of sheared vertex models [28].

The onset of probe motion depends on cell deformability, a measure of cell-edge tension. Near onset, velocity-force curves become sharper for rigid monolayers, and the probe's instantaneous velocity behaves differently. At high deformability, this velocity is sharply and evenly distributed around its mean as the probe smoothly squeezes through compliant neighboring cells, resulting in small local yield stress. At low deformability, the probe needs to displace cells within its vicinity to move, resulting in velocity distributions with fat tails and large local yield

stress. These differences correlate with the structural topology of the solidlike state, which is near crystalline for rigid cells, but glassy and defect-ridden for soft cells.

Model.—We describe a tissue monolayer using a multiphase field model with N cells, each represented by a scalar field $\phi_i(\boldsymbol{r})$. Phase field models incorporate cell shape deformation (a measure of tissue fluidity [15,17]) and allow for cell intercalation and density inhomogeneities, and they capture many properties of dense tissue layers [45,52,53]. The free energy of the system is given by

$$\mathcal{F} = \sum_{i=1}^{N}\left[\int d^2\boldsymbol{r}\left(\frac{\alpha}{4}\phi_i^2(\phi_i-\phi_0)^2+\frac{K}{2}(\boldsymbol{\nabla}\phi_i)^2\right)\right. \\ \left.+\lambda\left(1-\int d^2\boldsymbol{r}\frac{\phi_i^2}{\pi R^2\phi_0^2}\right)^2+\epsilon\sum_{i<j=1}^{N}\int d^2\boldsymbol{r}\,\phi_i^2\phi_j^2\right]. \quad (1)$$

The first term sets $\phi_0 = 2$ and 0 in the interior and exterior of each cell, respectively. The second term penalizes gradients in the phase with a stiffness K. These two terms determine the interfacial thickness $\xi = \sqrt{2K/\alpha}$ and the cell-edge tension $\sigma = \sqrt{8K\alpha/9}$, which is in turn controlled by cortex contractility and cell-cell adhesion. The third term is a soft constraint on the cell area, with the preferred area set to that of a circle of radius $R = 12$. Finally, the fourth term models steric repulsion ($\epsilon = 0.1$) by penalizing cell overlap.

Cell dynamics is overdamped due to friction with the substrate and is governed by the equation

$$\frac{\partial\phi_i}{\partial t}+\boldsymbol{v}_i\cdot\boldsymbol{\nabla}\phi_i = -\frac{1}{\gamma}\frac{\delta\mathcal{F}}{\delta\phi_i}, \quad (2)$$

where $\gamma = 10$ is an inverse mobility. Cell motility enters through advection by the cell self-propulsion velocity $\boldsymbol{v}_i = v_0(\cos\theta_i, \sin\theta_i)$. As in active Brownian particle models, we assume that, in isolation, all cells move at the same speed v_0, while the direction of motion θ_i is randomized by noise at rate D_r, $d\theta_i(t) = \sqrt{2D_r}dW_i(t)$, where $W_i(t)$ is a Wiener process and $D_r = 10^{-4}$. This minimal version of the model has been shown to capture the organization of epithelial monolayers [53]. We quantify cellular activity through the Péclet number $\mathrm{Pe} = v_0/(RD_r)$, with v_0/D_r the cells' persistence length. Both v_0 and D_r can be mapped to physical values via mean squared displacement (MSD) data of cells.

When cells interact, they may change their area (at a cost λ), overlap (cost $\epsilon\xi R$), or deform their perimeter and shape (cost σR). We quantify cell deformability via the dimensionless parameter $d = \epsilon\xi R/(\sigma R)$ and vary it from 0.3 to 6.0 by changing σ for fixed $\xi = 2$. The compressibility $\chi = \lambda/(\epsilon\xi R)$ characterizes the competition between area changes and overlap and is fixed to $\chi = 125/3$, giving polydisperse systems without cell overlap (physically corresponding to extrusion out of the plane in a cell monolayer [14]). Further details of implementing the model are discussed in Supplemental Material (SM) [54] and in [14].

We embed in the tissue a probe particle described by a rigid phase field ($d = 0.015, \chi = 2500$) of the same size as the cells and subject to the same free energy, so that it remains circular at all times. The probe is pulled at a constant force F along the x axis, and we measure its velocity as $v_b t = [x_b(t+\Delta t) - x_b(t)]/\Delta t$, with $x_b(t)$ the instantaneous x position of the probe, over intervals of $\Delta t = 0.01D_r^{-1}$ for a range of values of d and Pe.

We characterize the solidlike or liquidlike state of the system by studying the long-time behavior of cells' MSD, with $\mathrm{MSD}(t) \sim t^{\alpha}$ (see SM [54]). In the solidlike state the cells behave subdiffusively ($\alpha < 1$), whereas in the liquidlike state they move diffusively ($\alpha = 1$; Figs. S1 and S2 in SM [54]).

Threshold force and local yield stress.—In our solidlike tissues, a finite threshold force F_c is required for the probe to move at a nonzero velocity (Fig. 1). In colloidal suspensions, the threshold force probed by microrheology can be related quantitatively to the macroscopic yield stress [42]. While the detailed form of such a relation has not been established for the case of deformable particles, this suggests that the behavior of F_c should be at least qualitatively similar to that of the tissue yield stress.

A typical velocity-force curve for our rheological probe is shown in Fig. 1. We identify three dynamical regimes. At low forces, the probe rattles within its cage but is unable to escape (light brown region). At greater forces (green region), it deforms its neighbors strongly enough to escape the cage but can be temporarily trapped in new cages, resulting in stick-slip motion. As the force increases further, the probe no longer spends any time caged—its

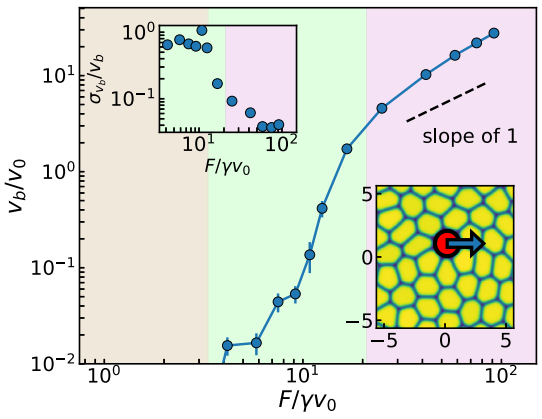

FIG. 1. A typical velocity-force curve for a hard probe particle in a glassy tissue [$(d, \mathrm{Pe}) = (3.0, 0.1)$] showing three dynamical regimes [from left to right: caging (brown), stick-slip (green), and moving freely (purple)]. Upper inset: the relative strength of the velocity fluctuations decreases above the critical force. Lower inset: a snapshot of the simulation setup.

instantaneous velocity becomes finite at all times, and the velocity-force curve turns almost linear. We identify the threshold force F_c as that at which the average long-time displacement of the bead's position $\Delta x_b = x_b(200D_r^{-1}) - x_b(20D_r^{-1})$ equals R. The precise choice of the cutoff, or a definition based on the long-time exponent with which displacement grows with time, does not affect the qualitative behavior of F_c as a function of Pe and deformability (Figs. S3–S5 [54]) [54]. Below F_c, the probe is either completely caged or engages in very rare stick-slip motion. Just above F_c, it instead moves substantially through the tissue, in frequent stick-slip or steady motion. The strength of velocity fluctuations relative to the mean decreases for $F > F_c$ (Fig. 1, upper inset), which is further evidence for a dynamical transition associated with local yielding.

To examine the effect of activity, we vary Pe at fixed deformability. The resulting velocity-force curves are shown in Fig. 2(a) for highly deformable cells ($d = 3.0$). Increasing activity leads to a smoother transition at the onset of motion. This is qualitatively similar to the thermal rounding observed in depinning phenomena [55], although in our system the probe velocity is zero over a finite range of applied forces for small Pe, indicating that the threshold force F_c is nonzero even in the presence of noise. Specifically, F_c and the associated local yield stress decrease with Pe, but remain finite within the precision of our simulations until Pe = 0.4 [Fig. 2(a), inset]. This is also the point at which the tissue melts, as shown by MSD data (Fig. S1 [54]), suggesting the existence of a finite local yield stress can be used to characterize the global solidlike or fluidlike state of the tissue.

To examine the effect of deformability, we fix Pe = 0.1 and vary d, such that the system remains solidlike for all values of d considered (Fig. S2 [54]). Figure 2(b) and SM Fig. S7 [54] show that the onset of motion changes qualitatively depending on cell-edge tension (or deformability). Tissues composed of cells with low tension are highly compliant and can adapt to the deformation induced by the probe simply through cell-shape changes. This gives a smooth, continuous onset of motion and low local yield stress. In contrast, rigid cells that resist deformation result in a sharp, almost discontinuous onset of motion and large local yield stress, as in this case the probe needs to push aside its neighbors to start moving. The decrease of threshold force with increasing deformability can be understood by assuming that $F_c \sim k_{\mathrm{eff}}$, where k_{eff} is the effective spring constant felt by a caged particle. A calculation shows that $k_{\mathrm{eff}} \sim 1/d$ (see SM [54]), consistent with data shown in the inset of Fig. 2(b). A more detailed analysis may require considering many-body interactions, as in foams [56]. The qualitative difference in the behavior at low and high deformability becomes apparent when plotting histograms of the probe's instantaneous velocities, which are much broader and exhibit fatter tails for low d, especially in the vicinity of F_c [Figs. 2(c)–2(f) and S8 [54]].

Deformation patterns close to the probe.—As the probe is dragged around the tissue, it can substantially deform cells nearby. To quantify the extent of such deformations, we consider the deformation tensor $\boldsymbol{S}_i$ [45], where

$$S_{i,\alpha\beta} = -\int d^2\boldsymbol{r}\left[(\partial_\alpha\phi_i)(\partial_\beta\phi_i) - \frac{\delta_{\alpha\beta}}{2}(\partial_\gamma\phi_i)^2\right]. \quad (3)$$

This tensor has eigenvectors $\hat{\boldsymbol{n}}_i^e$ and $\hat{\boldsymbol{n}}_i^c$ with eigenvalues s_i and $-s_i$, respectively, where $s_i = \sqrt{S_{i,xx}^2 + S_{i,xy}^2}$ gives the magnitude of the deformation. $\hat{\boldsymbol{n}}_i^e = (\sin\varphi_i, -\cos\varphi_i)$ points along the axis of greatest elongation, whereas

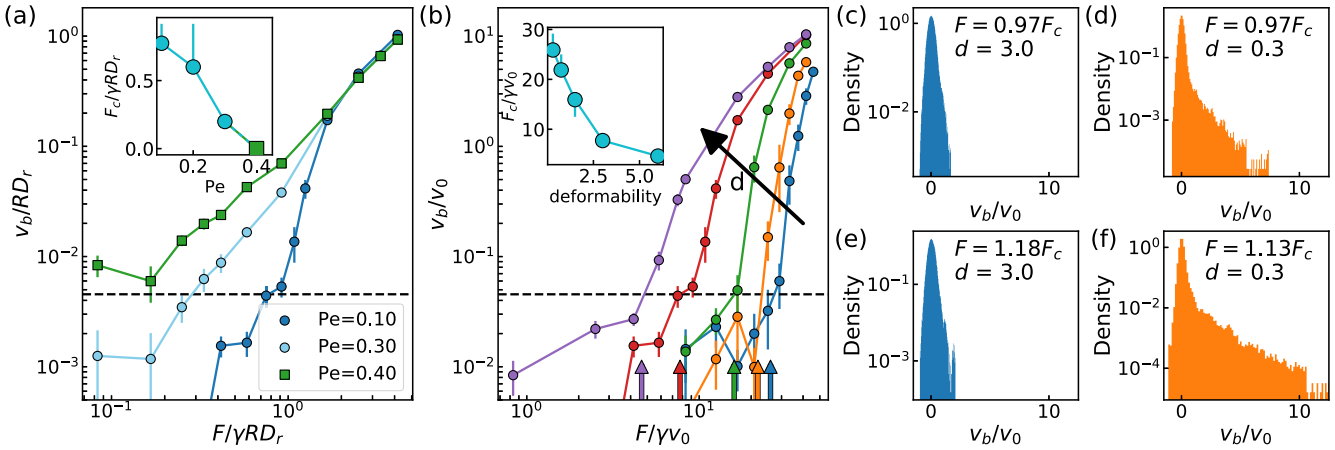

FIG. 2. Probe velocity v_b versus applied force F from varying cell motility and deformability. (a) Velocity-force curves at high deformability ($d = 3.0$) versus Pe. Inset: the threshold force F_c versus Pe. Circles denote a glassy state with a subdiffusive MSD, whereas squares indicate a liquid system with a diffusive MSD. (b) Velocity-force curves at Pe = 0.1 for various deformability ($d = 0.3$, 0.75, 1.5, 3.0, and 6.0). Inset: F_c versus d. All points correspond to the tissue being in a glassy state. (c)–(f) Normalized histograms of v_b for $d = 3.0$ and 0.3 for forces F just below and above F_c. The values above F_c are chosen as close as possible to give comparable values of F/F_c.

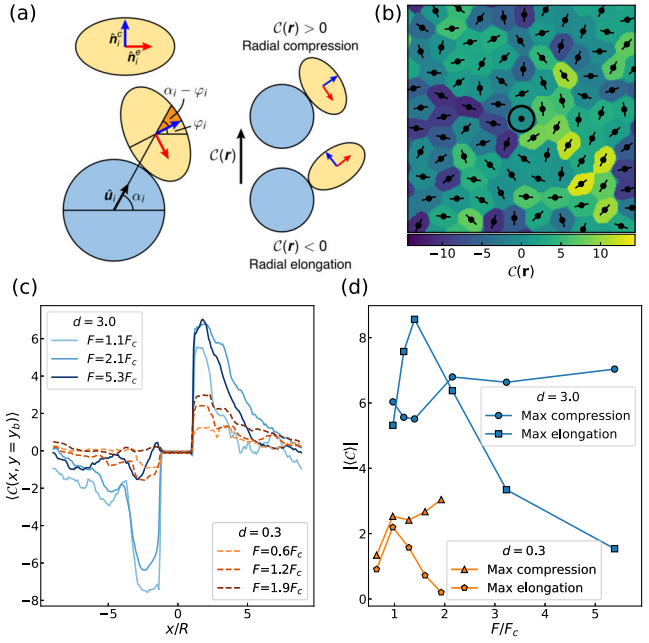

FIG. 3. Quantifying cell deformation around the probe. (a) Schematics explaining the radial compression field $\mathcal{C}(\boldsymbol{r})$, computed based on the alignment of the cell compression axis $\hat{\boldsymbol{n}}_i^c$ with the vector $\hat{\boldsymbol{u}}_i$ pointing from the center of the probe (blue) to that of the cell (yellow). (b) Heat map of $\mathcal{C}(\boldsymbol{r})$ for $d = 3.0$, $\mathrm{Pe} = 0.1$, and $F = 0.93F_c$, showing the axis of cell elongation $\hat{\boldsymbol{n}}_i^e$. (c) Profiles of $\mathcal{C}(\boldsymbol{r})$ along the probe's center in the x direction, i.e., $\langle \mathcal{C}(x, y = y_b) \rangle$, for $d = 0.3$ and 3.0 with $\mathrm{Pe} = 0.1$. (d) Absolute values of the minima and maxima of $\langle \mathcal{C}(x, y = y_b) \rangle$ versus F for parameters as in (c).

$\hat{\boldsymbol{n}}_i^c = (\cos\varphi_i, \sin\varphi_i)$ is along the axis of greatest compression, and φ_i is the angle between $\hat{\boldsymbol{n}}_i^c$ and the x axis [Fig. 3(a)]. Using this tensor, we measure the degree of deformation of each cell in the direction from the probe by defining the radial compression field

$$\mathcal{C}(\boldsymbol{r}) = \sum_i s_i H[\phi_i(\boldsymbol{r}) - \phi_0/2] \cos[2(\alpha_i - \varphi_i)], \quad (4)$$

where H is the Heaviside function and the field is smoothed to interpolate values on cell boundaries. Here, α_i is defined by the vector $\hat{\boldsymbol{u}}_i = (\cos\alpha_i, \sin\alpha_i)$ pointing from the center of the probe to that of cell i. Positive or negative values of $\mathcal{C}(\boldsymbol{r})$, respectively, signify local compression or elongation along $\boldsymbol{r}$. Figure 3(b) shows a snapshot of $\mathcal{C}(\boldsymbol{r})$, indicating a buildup of compression along x in front of the probe and a wake of elongation behind. The latter is reminiscent of the density voids found in the wake of a colloidal probe dragged through granular materials [57–63], suspensions of active hard spheres [40,41], colloidal suspensions [64–66], and foams [67].

Compression and elongation are largest at about one cell length from the probe, independent of F [Fig. 3(c)], and the magnitude of the deformation increases with d. While compression remains roughly constant beyond F_c, as the probe only requires enough of a compression to escape its cage, the magnitude of elongation behind the probe is nonmonotonic with F [Fig. 3(d)]. This behavior arises because elongation requires the probe to create free space where the cells behind it can expand. When the probe undergoes stick-slip motion, the large instantaneous forces create empty regions behind it. Instead, when the probe moves freely, the cells behind it follow the motion smoothly, hence their elongation decreases. The maximum elongation is found just at F_c for the low d case, but further away for high d, consistent with the former being a sharper transition, where the transitional stick-slip regime is narrower.

Defect statistics and topological healing.—To identify the physical mechanisms underlying the behavior at different deformability, we analyze the topological structure of cell center packing in the solidlike state. Figures 4 and S9 [54] show that defects obtained by Delaunay triangulation of the cell centers of mass are strikingly different at different d. The system is more ordered for rigid than for deformable cells, and defects are rarer in the former case [Figs. S10(a) and S10(b) [54]]. This is because at small d, cells try to minimize their perimeter by forming hexagonal shapes that can tile the plane regularly, whereas at high d, shape changes lead to a wider repertoire of possible emerging amorphous structures.

At all values of deformability, the probe's motion heals the system, reducing the number of defects over

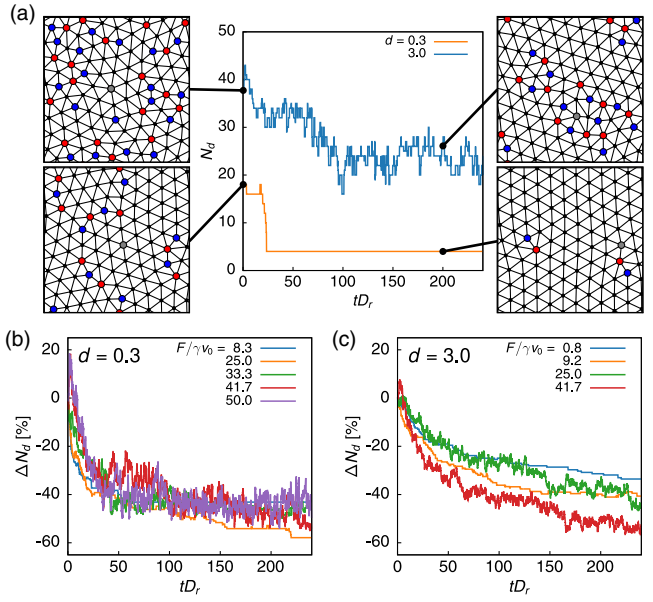

FIG. 4. Reduction in the number of disclinations N_d within the system over time at different deformability d. (a) Example time series of N_d for $d = 0.3$ and 3.0. Snapshots show the Delaunay triangulation of the system at $tD_r = 0$ and 200. Fivefold and sevenfold disclinations are shown as blue and red circles, respectively, and the probe particle marked in gray. (b) and (c) Time series showing the percentage change in N_d over time at various F for (b) $d = 0.3$ and (c) $d = 3.0$.

time [Figs. 4(b) and 4(c) and SM Fig. S10(a) [54]]. The timescales associated with this topological healing, however, depend on deformability and are smaller for low d. Again, this points to a sharper transition for rigid monolayers, and to a more compliant response of softer ones. While the probe heals the system locally, global healing can be achieved by increasing activity [Figs. S10(c) and S10(d) [54]]. The free motion of the probe therefore acts as noise in the system. The behavior is qualitatively similar to that of two-dimensional extended systems pinned by quenched disorder, where a uniform external drive first depins the system, setting it into motion, and then heals it at large applied forces, restoring partial translational order [68,69].

To conclude, we used simulations to probe the local mechanics in model cell monolayers. We found that the monolayer responds to local deformations like a yield-stress material even in the presence of noisy cell motility. We also showed that there is a fundamental relationship between the nature of the local yielding transition and microscopic cell properties such as cell-edge tension, as captured here by deformability, and cell motility. In monolayers of rigid cells local yielding requires cell displacement, resulting in a large threshold force. In contrast, monolayers of soft cells are compliant and yield locally through cell deformation [70], resulting in a smaller threshold force. As the surface tension of cancerous cells is thought to be larger than that of healthy tissues, these results suggest that intratissue dynamics may change significantly in disease, and it would be of interest to test this prediction experimentally—e.g., modifying σ by blebbistatin or cadherin knockouts. Our results are also relevant to recent dynamical measurements in *Drosophila* embryos based on embedding a probe inside a cell [38], or ferroelectric droplets in between neighboring cells [13], which suggest that local probes can provide quantitative information on local tissue rheology *in vivo*.

The work by A. H. and M. C. M. was supported by the National Science Foundation Grant No. DMR-1720256 (iSuperSeed) with additional support from DMR-2041459. This research has received funding (B. L.) from the European Research Council under the European Union's Horizon 2020 research and innovation programme (Grant Agreement No. 851196). Use was made of computational facilities purchased with funds from the National Science Foundation (CNS-1725797) and administered by the Center for Scientific Computing (CSC). The CSC is supported by the California NanoSystems Institute and the Materials Research Science and Engineering Center (MRSEC; NSF DMR 1720256) at UC Santa Barbara.

*Corresponding author.
austinhopkins@ucsb.edu

[1] M. Chuai, D. Hughes, and C. J. Weijer, Collective epithelial and mesenchymal cell migration during gastrulation, Curr. Genomics **13**, 267 (2012).

[2] A. Haeger, M. Krause, K. Wolf, and P. Friedl, Cell jamming: Collective invasion of mesenchymal tumor cells imposed by tissue confinement, Biochim. Biophys. Acta **1840**, 2386 (2014).

[3] M. Poujade, E. Grasland-Mongrain, A. Hertzog, J. Jouanneau, P. Chavrier, B. Ladoux, A. Buguin, and P. Silberzan, Collective migration of an epithelial monolayer in response to a model wound, Proc. Natl. Acad. Sci. U.S.A. **104**, 15988 (2007).

[4] J. P. Thiery, H. Acloque, R. Y. Huang, and M. A. Nieto, Epithelial-mesenchymal transitions in development and disease, Cell **139**, 871 (2009).

[5] E. W. Thompson and D. F. Newgreen, Carcinoma invasion and metastasis: A role for epithelial-mesenchymal transition?, Cancer Res. **65**, 5991 (2005).

[6] J. A. Mitchel, A. Das, M. J. O'Sullivan, I. T. Stancil, S. J. DeCamp, S. Koehler, O. H. Ocaña, J. P. Butler, J. J. Fredberg, M. A. Nieto, D. Bi, and J. A. Park, In primary airway epithelial cells, the unjamming transition is distinct from the epithelial-to-mesenchymal transition, Nat. Commun. **11**, 5053 (2020).

[7] L. Atia, D. Bi, Y. Sharma, J. A. Mitchel, B. Gweon, S. A. Koehler, S. J. Decamp, B. Lan, J. H. Kim, R. Hirsch, A. F. Pegoraro, K. H. Lee, J. R. Starr, D. A. Weitz, A. C. Martin, J. A. Park, J. P. Butler, and J. J. Fredberg, Geometric constraints during epithelial jamming, Nat. Phys. **14**, 613 (2018).

[8] C. Malinverno *et al.*, Endocytic reawakening of motility in jammed epithelia, Nat. Mater. **16**, 587 (2017).

[9] S. Garcia, E. Hannezo, J. Elgeti, J.-F. Joanny, P. Silberzan, and N. S. Gov, Physics of active jamming during collective cellular motion in a monolayer, Proc. Natl. Acad. Sci. U.S.A. **112**, 15314 (2015).

[10] J. A. Park *et al.*, Unjamming and cell shape in the asthmatic airway epithelium, Nat. Mater. **14**, 1040 (2015).

[11] K. D. Nnetu, M. Knorr, J. Käs, and M. Zink, The impact of jamming on boundaries of collectively moving weak-interacting cells, New J. Phys. **14**, 115012 (2012).

[12] T. E. Angelini, E. Hannezo, X. Trepat, M. Marquez, J. J. Fredberg, and D. A. Weitz, Glass-like dynamics of collective cell migration, Proc. Natl. Acad. Sci. U.S.A. **108**, 4714 (2011).

[13] A. Mongera, P. Rowghanian, H. J. Gustafson, E. Shelton, D. A. Kealhofer, E. K. Carn, F. Serwane, A. A. Lucio, J. Giammona, and O. Campàs, A fluid-to-solid jamming transition underlies vertebrate body axis elongation, Nature (London) **561**, 401 (2018).

[14] B. Loewe, M. Chiang, D. Marenduzzo, and M. C. Marchetti, Solid-Liquid Transition of Deformable and Overlapping Active Particles, Phys. Rev. Lett. **125**, 038003 (2020).

[15] D. Bi, X. Yang, M. C. Marchetti, and M. L. Manning, Motility-Driven Glass and Jamming Transitions in Biological Tissues, Phys. Rev. X **6**, 021011 (2016).

[16] F. Giavazzi, M. Paoluzzi, M. Macchi, D. Bi, G. Scita, M. L. Manning, R. Cerbino, and M. C. Marchetti, Flocking transitions in confluent tissues, Soft Matter **14**, 3471 (2018).

[17] D. Bi, J. H. Lopez, J. M. Schwarz, and M. L. Manning, A density-independent rigidity transition in biological tissues, Nat. Phys. **11**, 1074 (2015).

[18] D. L. Barton, S. Henkes, C. J. Weijer, and R. Sknepnek, Active vertex model for cell-resolution description of epithelial tissue mechanics, PLoS Comput. Biol. **13**, e1005569 (2017).
[19] Y.-W. Li and M. P. Ciamarra, Role of cell deformability in the two-dimensional melting of biological tissues, Phys. Rev. Mater. **2**, 045602 (2018).
[20] M. Chiang and D. Marenduzzo, Glass transitions in the cellular Potts model, Europhys. Lett. **116**, 28009 (2016).
[21] M. Durand and J. Heu, Thermally Driven Order-Disorder Transition in Two-Dimensional Soft Cellular Systems, Phys. Rev. Lett. **123**, 188001 (2019).
[22] P. Marmottant, A. Mgharbel, J. Kafer, B. Audren, J.-P. Rieu, J.-C. Vial, B. van der Sanden, A. F. M. Maree, F. Graner, and H. Delanoe-Ayari, The role of fluctuations and stress on the effective viscosity of cell aggregates, Proc. Natl. Acad. Sci. U.S.A. **106**, 17271 (2009).
[23] S. A. Sandersius, C. J. Weijer, and T. J. Newman, Emergent cell and tissue dynamics from subcellular modeling of active biomechanical processes, Phys. Biol. **8**, 045007 (2011).
[24] E. Sadeghipour, M. A. Garcia, W. J. Nelson, and B. L. Pruitt, Shear-induced damped oscillations in an epithelium depend on actomyosin contraction and E-cadherin cell adhesion, eLife **7**, e39640 (2018).
[25] S. Kim, M. Pochitaloff, G. A. Stooke-Vaughan, and O. Campàs, Embryonic tissues as active foams, Nat. Phys. **17**, 859 (2021).
[26] S. Tong, N. K. Singh, R. Sknepnek, and A. Kosmrlj, Linear viscoelastic properties of the vertex model for epithelial tissues, PLoS Comput. Biol. (2022).
[27] V. N. Prakash, M. S. Bull, and M. Prakash, Motility-induced fracture reveals a ductile-to-brittle crossover in a simple animal's epithelia, Nat. Phys. **17**, 504 (2021).
[28] J. Huang, J. O. Cochran, S. M. Fielding, M. C. Marchetti, and D. Bi, Shear-Driven Solidification and Nonlinear Elasticity in Epithelial Tissues, Phys. Rev. Lett. **128**, 178001 (2022).
[29] A. Hernandez, M. F. Staddon, M. J. Bowick, M. C. Marchetti, and M. Moshe, Anomalous elasticity of a cellular tissue vertex model, Phys. Rev. E **105**, 064611 (2022).
[30] J. H. Kim, X. Serra-Picamal, D. T. Tambe, E. H. Zhou, C. Y. Park, M. Sadati, J. A. Park, R. Krishnan, B. Gweon, E. Millet, J. P. Butler, X. Trepat, and J. J. Fredberg, Propulsion and navigation within the advancing monolayer sheet, Nat. Mater. **12**, 856 (2013).
[31] S. Tlili, M. Durande, C. Gay, B. Ladoux, F. Graner, and H. Delanoë-Ayari, Migrating Epithelial Monolayer Flows Like a Maxwell Viscoelastic Liquid, Phys. Rev. Lett. **125**, 088102 (2020).
[32] T. M. Squires and J. F. Brady, A simple paradigm for active and nonlinear microrheology, Phys. Fluids **17**, 073101 (2005).
[33] P. Habdas, D. Schaar, A. C. Levitt, and E. R. Weeks, Forced motion of a probe particle near the colloidal glass transition, Europhys. Lett. **67**, 477 (2004).
[34] L. G. Wilson, A. W. Harrison, A. B. Schofield, J. Arlt, and W. C. K. Poon, Passive and active microrheology of hard-sphere colloids, J. Phys. Chem. B **113**, 3806 (2009).
[35] A. M. Puertas and T. Voigtmann, Microrheology of colloidal systems, J. Phys. Condens. Matter **26**, 243101 (2014).
[36] M. Gruber, G. C. Abade, A. M. Puertas, and M. Fuchs, Active microrheology in a colloidal glass, Phys. Rev. E **94**, 042602 (2016).
[37] M. Gruber, A. M. Puertas, and M. Fuchs, Critical force in active microrheology, Phys. Rev. E **101**, 012612 (2020).
[38] A. D'Angelo, K. Dierkes, C. Carolis, G. Salbreux, and J. Solon, *In vivo* force application reveals a fast tissue softening and external friction increase during early embryogenesis, Curr. Biol. **29**, 1564 (2019).
[39] C. Reichhardt and C. J. Olson Reichhardt, Active microrheology in active matter systems: Mobility, intermittency, and avalanches, Phys. Rev. E **91**, 032313 (2015).
[40] E. W. Burkholder and J. F. Brady, Nonlinear microrheology of active Brownian suspensions, Soft Matter **16**, 1034 (2020).
[41] M. Knežević, L. E. Avilés Podgurski, and H. Stark, Oscillatory active microrheology of active suspensions, Sci. Rep. **11**, 22706 (2021).
[42] L. Mohan, M. Cloitre, and R. T. Bonnecaze, Active microrheology of soft particle glasses, J. Rheol. **58**, 1465 (2014).
[43] M. Nonomura, Study on multicellular systems using a phase field model, PLoS One **7**, e33501 (2012).
[44] B. Palmieri, Y. Bresler, D. Wirtz, and M. Grant, Multiple scale model for cell migration in monolayers: Elastic mismatch between cells enhances motility, Sci. Rep. **5**, 11745 (2015).
[45] R. Mueller, J. M. Yeomans, and A. Doostmohammadi, Emergence of Active Nematic Behavior in Monolayers of Isotropic Cells, Phys. Rev. Lett. **122**, 048004 (2019).
[46] G. Peyret, R. Mueller, J. D'Alessandro, S. Begnaud, P. Marcq, R. M. Mège, J. M. Yeomans, A. Doostmohammadi, and B. Ladoux, Sustained oscillations of epithelial cell sheets, Biophys. J. **117**, 464 (2019).
[47] G. Zhang, R. Mueller, A. Doostmohammadi, and J. M. Yeomans, Active inter-cellular forces in collective cell motility, J. R. Soc. Interface **17**, 20200312 (2020).
[48] D. Wenzel and A. Voigt, Multiphase field models for collective cell migration, Phys. Rev. E **104**, 054410 (2021).
[49] G. Zhang and J. M. Yeomans, Active forces in confluent cell monolayers, arXiv:2111.14401.
[50] S. Monfared, G. Ravichandran, J. E. Andrade, and A. Doostmohammadi, Mechanics of live cell elimination, arXiv:2108.07657.
[51] T. Vasilica Stirbat, S. Tlili, T. Houver, J.-P. Rieu, C. Barentin, and H. Delanoë-Ayari, Multicellular aggregates: A model system for tissue rheology, Eur. Phys. J. E **36**, 84 (2013).
[52] T. B. Saw, A. Doostmohammadi, V. Nier, L. Kocgozlu, S. Thampi, Y. Toyama, P. Marcq, C. T. Lim, J. M. Yeomans, and B. Ladoux, Topological defects in epithelia govern cell death and extrusion, Nature (London) **544**, 212 (2017).
[53] J.-M. Armengol-Collado, L. N. Carenza, J. Eckert, D. Krommydas, and L. Giomi, Epithelia are multiscale active liquid crystals, arXiv:2202.00668.
[54] See Supplemental Material at http://link.aps.org/supplemental/10.1103/PhysRevLett.129.148101 for additional simulation details, the derivation of the effective spring constant, and extended data complimenting the results in the main text.

[55] A. A. Middleton, Thermal rounding of the charge-density-wave depinning transition, Phys. Rev. B **45**, 9465 (1992).
[56] R. Höhler and S. Cohen-Addad, Many-body interactions in soft jammed materials, Soft Matter **13**, 1371 (2017).
[57] J. Pan, J. Chen, and J. Li, Dynamical behaviors of self-propulsion intruder buried in granular materials, Soft Matter **17**, 9997 (2021).
[58] P. Das, S. Puri, and M. Schwartz, Intruder dynamics in a frictional granular fluid: A molecular dynamics study, Phys. Rev. E **102**, 042905 (2020).
[59] Y. Zhang and R. Behringer, Pulling an intruder from a granular material: A novel depinning experiment, EPJ Web Conf. **140**, 4 (2017).
[60] A. Seguin, C. Coulais, F. Martinez, Y. Bertho, and P. Gondret, Local rheological measurements in the granular flow around an intruder, Phys. Rev. E **93**, 012904 (2016).
[61] E. Kolb, P. Cixous, N. Gaudouen, and T. Darnige, Rigid intruder inside a two-dimensional dense granular flow: Drag force and cavity formation, Phys. Rev. E **87**, 032207 (2013).
[62] R. Candelier and O. Dauchot, Creep Motion of an Intruder within a Granular Glass Close to Jamming, Phys. Rev. Lett. **103**, 128001 (2009).
[63] R. Candelier and O. Dauchot, Journey of an intruder through the fluidization and jamming transitions of a dense granular media, Phys. Rev. E **81**, 011304 (2010).
[64] R. N. Zia and J. F. Brady, Stress development, relaxation, and memory in colloidal dispersions: Transient nonlinear microrheology, J. Rheol. **57**, 457 (2013).
[65] I. C. Carpen and J. F. Brady, Microrheology of colloidal dispersions by Brownian dynamics simulations, J. Rheol. **49**, 1483 (2005).
[66] A. S. Khair and J. F. Brady, Microviscoelasticity of colloidal dispersions, J. Rheol. **49**, 1449 (2005).
[67] L. Viitanen, J. Koivisto, A. Puisto, M. Alava, and S. Santucci, Probing the local response of a two-dimensional liquid foam, Eur. Phys. J. B **92**, 38 (2019).
[68] T. Giamarchi and P. Le Doussal, Elastic Theory of Pinned Flux Lattices, Phys. Rev. Lett. **72**, 1530 (1994).
[69] L. Balents, M. C. Marchetti, and L. Radzihovsky, Non-equilibrium steady states of driven periodic media, Phys. Rev. B **57**, 7705 (1998).
[70] T. Fuhs, F. Wetzel, A. Fritsch, X. Li, R. Stange, S. Pawlizak, T. Kießling, E. Morawetz, S. Grosser, F. Sauer *et al.*, Rigid tumors contain soft cancer cells (2021), available at Research Square.